

A laboratory-numerical approach for modelling scale effects in dry granular slides

Abstract Granular slides are omnipresent in both natural and industrial contexts. Scale effects are changes in physical behaviour of a phenomenon at different geometric scales, such as between a laboratory experiment and a corresponding larger event observed in nature. These scale effects can be significant and can render models of small size inaccurate by underpredicting key characteristics such as flow velocity or runout distance. Although scale effects are highly relevant to granular slides due to the multiplicity of length and time scales in the flow, they are currently not well understood. A laboratory setup under Froude similarity has been developed, allowing dry granular slides to be investigated at a variety of scales, with a channel width configurable between 0.25 and 1.00 m. Maximum estimated grain Reynolds numbers, which quantify whether the drag force between a particle and the surrounding air act in a turbulent or viscous manner, are found in the range $10^2 - 10^3$. A discrete element method (DEM) simulation has also been developed, validated against an axisymmetric column collapse and a granular slide experiment of Hutter et al. (*Acta Mech* 109:127–165, 1995), before being used to model the present laboratory experiments and to examine a granular slide of significantly larger scale. This article discusses the details of this laboratory-numerical approach, with the main aim of examining scale effects related to the grain Reynolds number. Increasing dust formation with increasing scale may also exert influence on laboratory experiments. Overall, significant scale effects have been identified for characteristics such as flow velocity and runout distance in the physical experiments. While the numerical modelling shows good general agreement at the medium scale, it does not capture differences in behaviour seen at the smaller scale, highlighting the importance of physical models in capturing these scale effects.

Keywords Discrete element method · Froude scaling · Granular slides · Laboratory modelling · LIGGGHTS-DEM · Scale effects

Introduction

Granular slides and flows are common phenomena, not only in natural contexts such as landslides, avalanches, and pyroclastic flows (Pudasaini and Hutter 2010), but also in industrial applications such as chutes, hoppers, blenders, rotating drums (Turnbull 2011; Zhu et al. 2008), and heap formation (Bryant et al. 2014; Markauskas and Kačianauskas 2011; Zhang and Vu-Quoc 2000). Granular slides can be characterised as assemblies of discrete particles moving together relative to their surroundings with defined initial and final configurations, differing in this respect from continuous flows. These slides can be triggered by instabilities such as temperature changes in either the particles or the interstitial fluid (air, water, etc.), acoustic propagation, or direct mechanical action on the slide mass (Aradian et al. 2002; Juanico et al. 2008; Montrasio et al. 2016). Granular slides can cause catastrophic damage through their bulk motion (Haque et al. 2016), but they can also have drastic indirect effects, with slides impacting into bodies of water producing significant tsunamis (Heller et al. 2008). This can lead to secondary hazards such as unintentional dam

formation (Chang et al. 2011), dam overtopping (Yavari-Ramshe and Ataie-Ashtiani 2016), or flooding of nearby coastal areas or settlements (Glimsdal et al. 2016).

Meanwhile, scale effects can be identified in many situations, where the properties and behaviour of a phenomenon can change significantly as its scale changes. Scale effects are caused by differences in force ratios between a scaled model and the real-world observations. The Froude number (Fr), relating to the balance between inertial and gravity forces, is the most important force ratio governing the behaviour of granular slides (Choi et al. 2015). Thus, a scale series of experiments can be designed via a Froude scaling approach such that their geometries and kinematics produce granular slides with identical Fr values, eliminating the interplay of inertial and gravity forces as a source of scale effects. The grain Reynolds number (Re) quantifies the type of drag that particles experience against the surrounding air, such as turbulent or laminar flow, while the Cauchy (Ca) and Euler numbers (Eu) represent the influences of stiffness and pressure on the particles respectively. It is expected that between these three numbers, Re will be the dominant source of scale effects for granular slides.

Scale effects in experimental fluid mechanics have been analysed quite thoroughly, with Heller (2011) reviewing scale effects and limiting criteria in many scenarios. However, there has been relatively little research into the scalability of granular slides (Iverson 2015) and a lack of clear scale separation between the microscopic grain scale and macroscopic flow scale (Andreotti et al. 2013; Armanini 2013). Some of the main scale effects presently identified are the increased slide velocities and runout distances for extremely large events (Johnson et al. 2016; Parez and Aharonov 2015). Many have attributed these to secondary factors such as fluidisation via airflow (Savage and Hutter 1989) or acoustics (Collins and Melosh 2003), shear-dependent frictional behaviour (Liu et al. 2016), melt-induced self-lubrication (Erisman 1986), and fragmentation (Davies et al. 1999; Lucas et al. 2014). However, Parez and Aharonov (2015) refute this and state that this increased runout is mainly a product of the granular physics itself, particularly the spreading of mass from the release condition over time. Natural avalanches and landslides can be of extremely large scales and can affect vast areas (Xu et al. 2014), making physical modelling on larger scales an uncommon but not impossible feat (Iverson et al. 2010; McElwaine and Nishimura 2001). The implications of scale effects being incorrectly captured by smaller models are clear, with designs based on models that do not properly account for scale effects potentially being dangerous. Similarly, the identification and mitigation of scale effects in industrial contexts can result in more efficient systems (Grima and Wypych 2011), higher profits, and improved safety as scale effects can be taken into account during design and upscaling.

Discrete element method (DEM) was introduced by Cundall and Strack (1979) in dense granular flows, and further details on implementation issues and contact physics can be found in Zhu et al. (2007). One of the main advantages of DEM over more continuum-based models, such as depth-averaged models (Liu et al. 2016; Savage and Hutter 1989),

material-point method (Llano-Serna et al. 2016; Więckowski et al. 1999), and smoothed particle hydrodynamics (SPH) (Bui et al. 2008; Nguyen et al. 2017), is its ability to capture particle-scale interactions directly. This allows DEM to provide a better representation of phenomena based on particle shape, size, and relative movement to other particles, such as particle segregation, contact force transmission, dilute surface flow regimes, and jamming. DEM also allows extraction of micro-scale data such as individual particle velocities, precisely mapped travel paths, and packing densities that can be difficult to measure experimentally, allowing for deeper quantitative understanding of how the aforementioned phenomena inform the bulk behaviour of the granular slide. Averaging procedures can then be developed to extract other macro-scale information such as density, velocity, and stress data, allowing for direct comparison to continuum-based models (Zhu et al. 2008) and experiments that provide bulk measurements of these characteristics. DEM is thus highly versatile at capturing both dense and dilute phases of granular flows, as well as flows ranging from quasi-static to predominantly kinetic (Reddy and Kumaran 2010).

While DEM is quite a processing-intensive modelling technique, it proves to be increasingly accessible as computational power and code efficiency increase, with simulations of millions of particles completing in a timely manner on computing clusters. Spherical particles are commonly used due to low performance costs, but can fail to describe more complex shape effects such as interlocking or eccentric particle contacts without additional modelling techniques. More computationally expensive particle types such as ellipsoidal (Campbell 2011; Ouadfel 1998), polygonal (Latham and Munjiza 2004; Mirghasemi et al. 1997; Walton 1982; Wu and Cocks 2006), and potential particles (Houlsby 2009) have been investigated, while creating particles as multi-sphere clusters that are adjusted to match mass and centroid position (Zheng and Hryciw 2017) is another common approach for improving particle shape (Kruggel-Emden et al. 2008; Matsushima and Saomoto 1978;

Mollanouri Shamsi and Mirghasemi 2012; Wu et al. 2016). This study uses spherical particles with an additional rolling resistance model, as this allows the experimental geometry described herein to be simulated with correctly sized particles in a timely manner.

The aim of this study is to introduce, calibrate, and validate a new laboratory-numerical approach to quantify scale effects, with focus on confined chute flows. To accomplish this, a versatile laboratory setup has been built (Fig. 1) to interrogate key properties of these slides at a range of scales. Furthermore, a numerical simulation was calibrated and validated against an axisymmetric column collapse and a chute experiment of Hutter et al. (1995). This simulation was then used to model a scale series of new laboratory experiments using the aforementioned setup; by contrasting the idealised DEM results with experimental observations, information can be derived from both micro- and macro-scale data on which mechanisms may be responsible for scale effects. These new laboratory experiments and corresponding DEM form the main focus of this study, analysing dry, cohesionless granular slides and thereby excluding cohesion and surface tension effects.

Experimental design and methodology

The laboratory setup shown in Fig. 1 was designed with the main objective to investigate scale effects in granular slides, requiring highly repeatable experiments at different scales. These experiments form a Froude scale series that allows for easy direct comparison and quantification of scale effects. This scale series approach was made possible by using moveable acrylic sidewalls to vary the chute width, as well as having detachable curved transition zones and runout areas, while the substructure was mostly constructed from aluminium profiles (Fig. 1). The scale factor λ is defined as the ratio between a characteristic length in nature (or the largest experimental scale) and the corresponding length of the model. This setup was designed with $\lambda = 1$ for the largest scale experiment and $\lambda = 4$ for the smallest in the scale series. The inclined ramp surface has a maximum channel width of 1.0 m and a

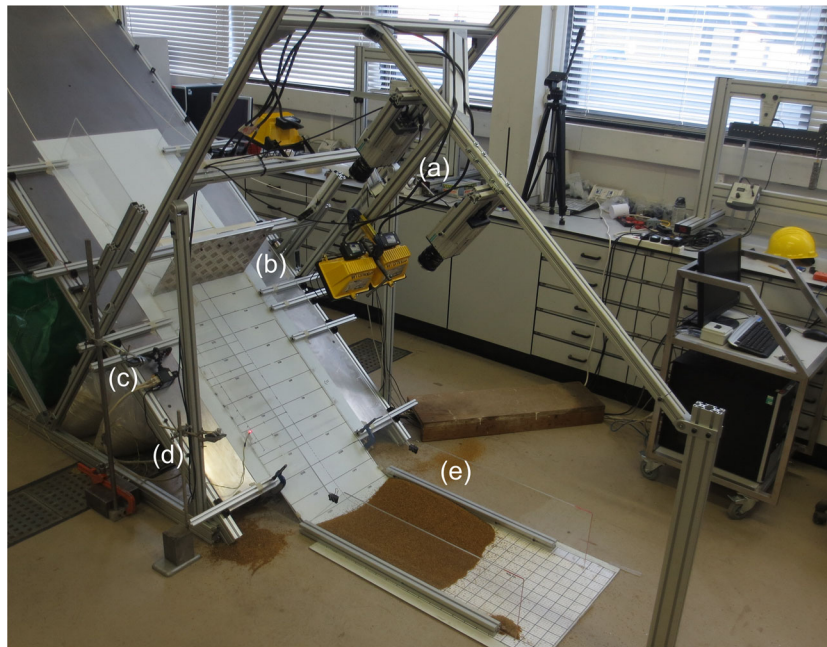


Fig. 1 Photograph of laboratory chute setup for medium-scale experiment ($\lambda = 2$), with (a) cameras at x_1 (top) and x_2 (bottom) for main recording of PIV footage, (b) rotating shutter, (c) camera at x_1 for recording of side footage for thickness measurement, (d) laser pointer at x_2 for calculation of slide thickness in central region, and (e) transition curve with deposit

total length of 3.0 m before it reaches the curved transition zone and subsequently runs out onto a flat area. The ramp angle θ_R is adjustable from $30^\circ - 60^\circ$ but was held constant at 40° in the presented experiments, as seen in Figs. 1 and 2. Furthermore, the slide release position can also be adjusted by fixing a shutter plate at different positions along the channel on a support bracket, and the rotation speed of the shutter can be controlled by attaching a counterweight at different positions. The slide is then triggered solely by the release of the shutter and its detachment from the slide mass.

Table 1 identifies key geometric parameters that vary between experiments, and Fig. 2 defines some further key parameters in relation to the ramp geometry. The x coordinate represents the direction along the ramp surface, with x_f , x_{max} and x_t representing the channel-wise positions of slide front, peak, and tail respectively. The y coordinate represents the cross-ramp direction with w being the channel width, while the z coordinate represents the direction perpendicular to the channel section at all times, with h_{max} denoting the maximum slide thickness along the channel centerline ($y=0$). The shutter counterweight system ensures that the shutter quickly detaches from the slide mass, accelerating away at an angular acceleration of ω_s for the duration of contact with the slide mass, in a highly consistent and repeatable manner between experiments at a given scale. This results in a shutter-tip velocity v_s after a rotation of 90° . $L_{s,0}$ and $H_{s,0}$ represent the initial slide wedge geometry, which can also be defined by a surface angle θ_w . V and M are the slide volume and mass. L_i denotes the distance between the shutter release point and the start of the transition curve, with radius R , while L_{sh} denotes the position of the shutter axis of rotation from the ramp surface. x_1 and x_2 relate to measurement positions from the shutter release point.

Garside Sands aggregate was graded to scale with the experiment, with grain diameters ranging from 0.5 to 1.0 mm (using 16/30 sand) for $\lambda = 4$, 1.0–2.0 mm (using 8/16 sand) for $\lambda = 2$, and 2.0–4.0 mm (using 5/8 sand) for $\lambda = 1$. d represents the mean grain diameter. Herein, the laboratory results at $\lambda = 2$ and 4 are presented. The angularity of these particles is very similar between all scales (with a ratio of 1.55 ± 0.05 between the major and minor axes), minimising differences in rolling

resistance and individual shape factors. The measured bed friction angle δ was identified by settling a pile of particles on a flat surface that was declined until the bulk mass started to mobilise. The internal friction angle ϕ was similarly measured by tilting a static cylinder of particles until the top surface started to mobilise. δ and ϕ were both $30 \pm 0.5^\circ$ for all of the sand samples.

Froude scaling was used to scale all relevant parameters such that experiments of different sizes could be compared quantitatively. By designing experiments such that they all share the same Froude number, we can ensure that the gravity force driving the slide has the same relative influence at all geometric scales. Thus, we can eliminate scale effects based on the Froude number. Accordingly, any differences seen in the slides at different scales must result from other factors that violate dynamic similarity, such as differences in the grain Reynolds number. In this study, the Froude number is defined as $Fr = u/\sqrt{gh}$, where u is the slide velocity and h is the slide thickness. h was chosen as a characteristic length for the slide in analogy to MiDi (2004) and Pouliquen and Forterre (2009), as it represents the criticality of the flow, providing insight into the influence of wave speed relative to flow-speed and general flow dynamics (Gray and Edwards 2014; Heller 2011).

To define the scale series, an initial Froude number was used with a characteristic velocity based on the potential energy of the slide. This results in $u_i = \sqrt{2gH_c}$, where H_c is the height of the mass centroid above the flat runout zone. The characteristic length is based on the mean initial slide height, $H_{s,0}/2$. The resulting Fr_i can thus be defined as $2\sqrt{H_c/H_{s,0}}$. The grain Reynolds number $Re = ud/\nu$ is a quantification of the type of particle-air interaction, where ν is the kinematic viscosity of the surrounding air ($15.11 \times 10^{-6} \text{ m}^2/\text{s}$). Similarly, the Cauchy number $Ca = \rho u^2/E$ parameterises the effects of particle compressibility on the slide dynamics, where E is the Young's modulus of the material (taken as 100 MPa). Notably, E has not been scaled linearly with λ after Froude scaling and may thus be a source of scale effects and result in increased dust formation at larger scales. The previous definition of u_i lets us define an initial grain Reynolds number $Re_i = \sqrt{2gH_c}d/\nu$ and initial Cauchy

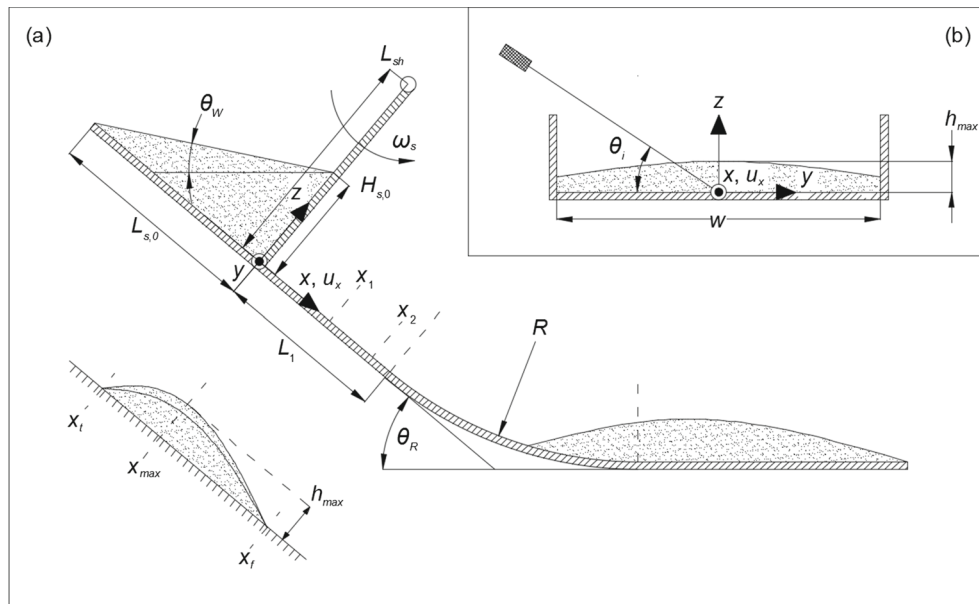


Fig. 2 Definition of bulk slide parameters. **a** Side view of the ramp, with x , y , z showing the curvilinear position coordinate system, and u_x being the rampwise velocity aligned with x . **b** Section of the slide across the channel width

Table 1 Key experimental parameters. Parameters kept constant between all experiments include the ramp inclination angle $\theta_R = 40^\circ$, the internal and bed friction angles $\delta = \phi = 30^\circ$, the grain density $\rho = 2640 \text{ kg/m}^3$, the simulated coefficient of restitution $e = 0.893$, and the grain stiffness $= 70 \text{ GPa}$

Exp. Numbers (-)	Exp. Type (-)	λ (-)	d (mm)	L_1 (m)	R (m)	L_{sl} (m)	ω_s (rad/s ²)	v_s (m/s)	w (m)
L1-L4	Laboratory	2	1.35	1.155	0.123	0.25	39.2	1.368	0.50
L5-L8	Laboratory	2	1.35	1.155	0.123	0.25	39.2	1.368	0.50
L9-L16	Laboratory	4	0.675	0.578	0.062	0.125	78.5	0.967	0.25
L17-L24	Laboratory	4	0.675	0.578	0.062	0.125	78.5	0.967	0.25
S1	Simulation	2	1.35	1.155	0.123	0.25	39.2	1.368	0.50
S2	Simulation	2	1.35	1.155	0.123	0.25	39.2	1.368	0.50
S3	Simulation	0.2	13.5	11.55	1.232	2.50	3.92	4.326	5.00

Exp. Numbers (-)	θ_{iv} ($^\circ$)	L_{s0} (m)	H_{s0} (m)	x_1 (m)	x_2 (m)	V (m ³)	M (kg)	f (Hz)
L1-L4	0	0.149	0.125	0.40	0.80	4.7×10^{-3}	7.374	1414
L5-L8	7.5	0.196	0.125	0.40	0.80	6.1×10^{-3}	9.712	1414
L9-L16	0	0.074	0.063	0.20	0.40	5.8×10^{-4}	0.922	2000
L17-L24	7.5	0.098	0.063	0.20	0.40	7.7×10^{-4}	1.214	2000
S1	0	0.149	0.125	0.40	0.80	4.7×10^{-3}	7.374	1414
S2	7.5	0.196	0.125	0.40	0.80	6.1×10^{-3}	9.712	1414
S3	0	1.490	1.250	4.00	8.00	4.655	7374.0	447

number $Ca_i = 2\rho gH_i/E$. Table 2 shows how these characteristic force ratios (Fr_i , Re_i , Ca_i) vary between the experiments. This demonstrates that Fr_i is constant between experiments of the same scale and initial slide shape, and any differences that appear as the slide develops may be attributed to scale effects.

The following highlights the relevance of Re in granular slides, with particle drag force being strongly influenced by the grain Reynolds number and representing its influence on the overall slide dynamics. Overall, the maximum drag force acting on a particle, assuming a conservative drag coefficient of 0.42 (for a spherical particle) and an estimated maximum velocity of 3 m/s at $\lambda = 2$, and using Rayleigh's drag force equation (Whitehead and Russell 1912), can reach almost 10% of the slope-normal gravitational force component. Most particles may experience less overall drag force due to air velocity approaching the slide velocity in the slide region. However, the particle angularity will cause the cross-sectional area to vary over time, introducing a significant fluctuating component to this drag force. Additionally, the non-sphericity of the particles may increase the drag coefficient drastically, with Loth (2008) evaluating this effect for multiple particle shapes. Re scale effects may further amplify or diminish the importance of this particle drag force on the slide dynamics, with small initial differences potentially cascading into large changes in overall behaviour. Furthermore, differences in Re between scales can correspond to differences in the relative turbulence of the air. This not only affects particles separated from the main slide mass by random collisions; it also affects the probability of this separation and the internal airflow through the bulk slide mass, possibly contributing to second-order effects that accumulate throughout the course of the slide event. Re is also a parametrisation of other frictional effects that may occur, such as fluidisation mechanisms.

The main measurements taken in the experiments are the rampwise surface velocities (u_s) measured at two distance intervals down the channel length (Table 1), as well as slide thickness at these points and measurements of the slide deposit. Measurements were taken only along the y -negative half of the chute given that the slide is symmetrical, using two high-speed cameras recording at a scale-specific frame rate (Table 1) and with a magnification factor of 0.042 between the image and object planes. The slide thickness was measured via two methods; at x_1 , a camera was used at the y -negative sidewall at 141 Hz, while at x_2 , a laser pointer was pointed at an angle of θ_i from the ramp surface (Fig. 2). This allowed the slide thickness to be calculated based on the horizontal distance of the laser point centre from its original position (the centre of the channel) via simple trigonometry. This method is based on Börzsönyi et al. (2009) and Saingier et al. (2016). The accuracy of coordinates taken from the ramp is estimated at $\pm 2.5\%$, due to parallax and positioning uncertainty, while the accuracy of the laser displacement method is estimated at $\pm 5\%$ due to occasional interference from stray particles blocking the line-of-sight, spreading the laser point over a wider strip of the channel width than the desired single point.

The camera footage from the two main cameras was analysed via particle image velocimetry (PIV) using DigiFlow software (Dalziel 2009) to produce velocity vectors across a 512×1024 pixel grid (in the respective x and y directions) at each camera position, with each vector representing an interrogation window (IW) of 45×45 pixels² (12.5×12.5 mm²). As the cameras recorded a slightly larger object area than the area to be analysed, 11×21 vectors resulted. Using a conservative estimate of a maximum measured slide velocity of 3 m/s, at the given frame rate in Table 1, this resulted in a maximum particle velocity of

Table 2 Initial (Fr_i , Re_i , and Ca_i) and measured (Fr , Re , and Ca) force ratios for conducted experiments. Measured force ratios are calculated at $t = 400$ camera frames after the slide front arrives at x_2

Exp. numbers (-)	λ (-)	H_i (m)	u_i (m/s)	Fr_i (-)	Re_i (-)	Ca_i (-)	u_s (m/s)	h_{max} (m)	Fr (-)	Re (-)	Ca (-)
L1-L4	2	0.830	4.04	5.15	401	4.32×10^{-4}	2.06	0.0088	7.01	205	1.12×10^{-4}
L5-L8	2	0.840	4.06	5.18	403	4.37×10^{-4}	2.11	0.0094	6.95	209	1.18×10^{-4}
L9-L16	4	0.415	2.85	5.15	142	2.16×10^{-4}	1.28	0.0052	5.67	64	4.34×10^{-5}
L17-L24	4	0.420	2.87	5.18	142	2.19×10^{-4}	1.20	0.0059	4.99	60	3.82×10^{-5}
S1	2	0.830	4.04	5.15	401	4.32×10^{-4}	2.11	0.0080	7.53	209	1.18×10^{-4}
S2	2	0.840	4.06	5.18	403	4.37×10^{-4}	2.17	0.0102	6.86	215	1.25×10^{-4}
S3	0.2	8.301	12.76	5.15	12,669	4.32×10^{-3}	6.67	0.0802	7.53	6624	1.18×10^{-3}

2.1 mm/frame, or 7.5 pixels/frame. As a result, most particles stayed within their respective IW during each iteration of the PIV analysis, allowing for stable vectors to be calculated reliably. The PIV algorithm completed three forward passes and one reverse subpixel pass to ensure that the correlation difference function between successive camera frames was minimised. This provided the best fit between the calculated velocity vectors for each IW and the overall shift of the camera images. Outlier vectors (greater than $1.2 \times$ the median vector value compared to adjacent vectors) and vectors generated from windows with insufficient intensity range or texture were replaced with interpolated values. Roughly 5% of the vectors were replaced by this procedure, which was deemed satisfactory in comparison to other studies (Eckart et al. 2003; Thielicke and Stamhuis 2014).

Deposit surface dimensions were measured photogrammetrically using AgiSoft PhotoScan software (AgiSoft-LLC 2016). The technique assembled a dense point cloud by matching common reference points between 10 and 20 images taken from different angles. Clear reference points were marked out throughout the chute runout zone and on the base of the column collapse test to allow a local coordinate system to be easily applied to the images. Mild depth filtering was used so that the roughness of the surface was preserved. This resulted in geometric models corresponding to the real deposit dimensions with an estimated measurement accuracy of ± 0.5 mm. The packing density of the deposit was calculated by dividing the measured slide mass by the slide volume estimated by the surface of the photogrammetric mesh, and then by dividing this by the particle density ρ . This could then be subtracted from unity to get the mean porosity n of the laboratory deposit.

LIGGGHTS-DEM: Model description

The DEM simulations used the Large-scale atomic/molecular massively parallel simulator Improved for General Granular and Granular Heat Transfer Simulations (LIGGGHTS) code from Kloss et al. (2012). This implementation of DEM used a Lagrangian method to explicitly solve particle trajectories throughout the domain. Particle-particle and particle-wall contacts were modelled using a linear spring-dashpot model that determined the normal (F_n) and tangential (F_t) contact forces through their respective spring (k_n and k_t) and damping (γ_n and γ_t) coefficients. These coefficients were calculated from properties such as the Young's Modulus, the Shear Modulus, the Poisson ratio, the restitution (relating to how much kinetic energy is dissipated during a collision), and friction (representing the ratio of the friction force and the normal force acting on the contact) coefficients via the Hertz contact model (Hertz 1882). The exact expressions used to define these spring and damping coefficients can vary, but the expressions used in this implementation of LIGGGHTS can be found in LIGGGHTS (2016). The normal force is given by

$$F_n = -k_n \delta_n + \gamma_n \Delta u_n, \quad (1)$$

while the magnitude of the tangential contact force is given by

$$F_t = \min \left\{ |k_t \int_{t_c}^t \Delta u_t dt + \gamma_t \Delta u_t|, \mu F_n \right\}. \quad (2)$$

During collisions, particles were allowed to overlap slightly, with the corresponding repulsive forces between particles being determined by the overlap distance (δ_n being the normal component) and the respective contact normal velocity vector Δu_n , while Δu_t is the corresponding tangential velocity vector (Kloss et al. 2012). In Eq. (2), the integral term

describes a spring that stores the energy of the relative tangential motion between particles, representing the elastic tangential deformation of the particle surfaces since the contact time $t = t_{c0}$, while the second part describes the energy dissipation of the tangential contact itself. The tangential overlap distance was curtailed to meet the Coulomb friction criterion for a friction coefficient of μ . The force balance was evaluated for each particle by summing F_n and F_t with the remaining body force vector F_b (including gravity, magnetic, and electrostatic forces), given by

$$m\mathbf{a} = F_n + F_t + F_b \quad (3)$$

and

$$I \frac{d\boldsymbol{\omega}}{dt} = \Sigma(\mathbf{r}_c \times \mathbf{F}_t) + T_r \quad (4)$$

respectively for each specific particle. In this study, the additional force vector exerted by the surrounding fluid is zero. m denotes the particle mass while \mathbf{a} denotes the particle translational acceleration vector. I denotes the particle moment of inertia, while $\boldsymbol{\omega}$ denotes the particle rotational velocity vector and \mathbf{r}_c denotes the contact radius vector. The momentum balance seen in Eq. (3) thus defines the angular and translational particle accelerations. While this approach is an approximation of real behaviour (real particles do not overlap, for instance), it is adequate for describing the most relevant and important particle behaviour accurately.

Two of the most common ways of incorporating particle angularity effects in a DEM are by combining several particles into clumps, or by adopting a "rolling friction" parameter for spherical grains (Wensrich and Katterfeld 2012). The major drawback of the particle clump approach is that, by using several particles to simulate each actual particle, the number of actual particles that can be simulated is greatly reduced due to limits in computational resources. In this study, simulating the correct particle count that matches the experiments (in particular ensuring that the non-dimensionalised slide thickness h/d scaled correctly throughout each slide event) was deemed more important than particle shape effects, so the "rolling friction" approach was used. Particle sphericity, defined as the ratio of a normalised particle radius to the radius of a circumscribing sphere (Wadell 1932), and angularity, defined as the number and sharpness of corners on the particle surface (Sukumaran and Ashmawy 2001), were thus modelled by applying rolling friction as a torque T_r to particles in collision, either with each other or a surface. A coefficient of rolling resistance μ_r has a physical basis in the mean eccentricity of a particle contact from its mass centroid, and is defined as the tangent of the angle at which the rolling resistance torque T_r is balanced by the torque produced by gravity acting on the particle (Ai et al. 2011). This torque is the sum of a mechanical spring torque T_r^k and a viscous damping torque T_r^d , and the maximum magnitude of the rolling resistance torque is given by

$$T_{r,max} = \mu_r R_r |F_n| \quad (5)$$

where R_r is the effective rolling radius of the particle contact. The value of μ_r could be adjusted to best describe the angularity and sphericity of particles used, increasing with particles with sharper contacts and decreasing with more spherical ones. However, T_r always acts against the direction of rotation, resulting in a slight overestimate of rolling resistance compared to actual non-

spherical particles. Nevertheless, it models the bulk effects of particle sphericity fairly well (Wensrich and Katterfeld 2012). A rolling viscous damping ratio η_r is similarly calibrated to adjust the importance of T_r^d in the rolling resistance model.

Contacts are detected via periodically constructed neighbour lists, which are checked and evaluated based on actual contacts at each timestep, excluding particle pairs that are too distant to have any interaction based on the Verlet parameter (Verlet 1967). In this study, the distance at which particle collisions start to be considered was set to two particle diameters, which achieved a good balance between suitability and performance. The size distribution of particles was modelled using a Gaussian distribution with a mean and standard deviation as close as possible to that of the experimental particles for each scale (i.e. 1.35 and 0.2 mm respectively at $\lambda = 2$). Preliminary simulations performed using monodisperse particles at the mean diameter were insufficient for modelling the slide behaviour (in particular during the deposition phase) and the laboratory deposit shape, justifying the use of the polydisperse approach. The packing method of the release wedge could also have a large effect on bulk dynamics; thus, particles were gravity deposited in the simulation to match the experimental pre-release conditions as closely as possible, such as the coordination number and radial distribution function (Liu 2003; Silbert et al. 2002; Yu et al. 2006).

The particle count n_p and timestep t_s of the chute slides, along with the settlement time in the simulation (T_s) and in real life ($T_{s,real}$), as well as the respective runout completion times (T_r) and ($T_{r,real}$), are shown in Table 3. An important model effect was the choice of t_s and how it varied at different scales. The stability of DEM calculations necessitates a timestep near or below the Rayleigh wave speed (Thornton 2015; Zhao 2017) of the particles. As this quantity is proportional to d , the timestep must also be proportional to d . Following Froude scaling by keeping the timestep proportional to u would result in incorrect kinetic energy calculations, violating conservation of energy. Accordingly, this means that small-scale simulations must take a larger number of timesteps to complete to ensure that no model effects are present in a scale series.

The porosity n of the simulated slide was calculated via a Monte-Carlo volume estimation method of assigning random points and noting whether they intersect particles (Wensrich and Katterfeld 2012), where the slide was linearised and split into a grid of cubic sub-regions. Particles that overlapped with a sub-region were factored into a local porosity calculation, with a point cloud being generated to fill the region with a specified number of points (in this case 100,000). Points that remained outside of any particles were deleted, and the porosity of the region was simply calculated as the ratio of deleted points to initial points generated. This method provided information on the spatial distribution of porosity throughout the slide at any given timestep.

The cylinder test contained 658,000 particles and used 12 Dell C6220 computing nodes of 32GB of RAM, each with 2×8 -core processors (Intel Sandybridge E5-2670 2.6 GHz) and a Message Passing Interface

(MPI) thread for each core. These 192 processors were assigned in a $12 \times 16 \times 1$ grid, representing tall vertical columns dividing the cylinder domain. The simulation time T_s required for the column to settle correctly via gravity deposition was 0.042 s (corresponding to a real time $T_{s,real}$ of 4.63 h) while the duration T_r of the collapse itself was 0.566 s (with $T_{r,real} = 37.56$ h). The corresponding timings for the chute tests can be seen in Table 3, with six computing nodes (a total of 96 processors) being arranged in a $1 \times 96 \times 1$ grid in the xyz coordinate system. The chute geometry allowed the processors to be divided in a way that ensured each domain was filled with an equal amount of particles, resulting in greater efficiency than the cylinder test.

Calibration and validation

Axisymmetric column collapse

Calibration of the LIGGGHTS code was conducted with an axisymmetric column collapse test, using a clear plastic cylinder that was raised rapidly via a pulley system. Many studies have been completed analysing the dynamics of two-dimensional column collapses confined by side-walls, as well as the cylindrical case without sidewalls evaluated here, using a variety of measurement techniques (Cleary and Frank 2006; Lajeunesse et al. 2004; Lube et al. 2004; Thompson and Huppert 2007; Warnett et al. 2014). While Grima and Wypych (2011) describe a more complex setup using a separating clamshell system to initiate the collapse, the simplicity of the vertical cylinder was preferred in this study. The cylinder had an internal diameter of 100 mm and was filled to a height of 200 mm using the same particles used for the main chute tests ($\lambda = 2$, $d = 1.35$ mm). This geometry was deemed suitable as it developed a sufficiently thick flow that produced Bagnold-like (Bagnold 1954) velocity profiles in the regions above the static central core. The setup also captured important flow features such as creep underneath a moving boundary, the development of shear flow, and an unconfined runout area. The column collapse itself was recorded at 1414 Hz, matching the corresponding frame rate for the chute experiments (Table 1).

Figure 3 shows a comparison between the calculated surface of one of the laboratory column collapse deposits and the simulation, which used typical values of $\mu_r = \eta_r = 0.30$ to model the rolling resistance and $e = 0.893$ as the coefficient of restitution. The laboratory deposit surface was extracted using the photogrammetry technique described in the methodology. It can be seen in Fig. 3 that the simulated angle of repose at both the top of the pile (20.7°) and towards the outer edge (9.5°) matches very well to the experimental result (20.1° and 9.9° respectively). The main difference is a larger extent of the outer rim, which is a consequence of the very dilute deposit in this region mostly consisting of a single-particle thick layer spreading out away from the main mass. This phenomenon is believed to be an artifact of using a rolling resistance coefficient to model particle angularity and sphericity; while this method captures the bulk energy transfer throughout the material well, the spherical particles are still able to roll out on a flat surface to a greater extent than real rough particles.

Table 3 Key DEM parameters

Exp. number (-)	Exp. type (-)	λ (-)	n_p (-)	T_s (s)	$T_{s,real}$ (hours)	T_r (s)	$T_{r,real}$ (hours)	t_s (s)
S1	Simulation	2	1.94×10^6	0.077	6.959	1.711	113.89	1.77×10^{-7}
S2	Simulation	2	2.55×10^6	0.127	19.188	1.725	152.93	1.77×10^{-7}
S3	Simulation	0.2	1.94×10^6	0.268	2.935	5.367	45.01	1.77×10^{-6}

Figure 4 more closely compares the simulated and experimental cylinder collapse events over time, with Fig. 4c highlighting the dilute outer rim region. Overall, the time evolution of the simulated and experimental column collapse matches reasonably well, with some minor differences due to the more uniform cylinder acceleration in the simulation and some minor electrostatic effects in the laboratory capturing some loose particles from the free surface. The main difference seen in Fig. 4 is that the granular column seems to collapse slightly faster in the simulation. However, given that the dimensions of the main pile body remain very close between laboratory and numerical experiments, and the excellent agreement of the angle of repose, $\mu_r = \eta_r = 0.30$ and $e = 0.893$ were deemed representative values for the granular material and were thus used in the main tests. The rolling resistance coefficient and rolling viscous damping ratio are the only relevant free simulation parameters that can be changed (e showed little sensitivity).

Comparisons to experiment 117 of Hutter et al. (1995)

The LIGGGHTS code was further validated against experiment 117 from Hutter et al. (1995), which is suitable for calibrating models (Banton et al. 2009). The release wedge used in Hutter et al. (1995) was 0.10 m wide and 0.20 m high at the shutter, causing sidewall friction to play an important part in the slide dynamics. This slide consisted of 4.00 kg of smooth glass beads of $d = 0.003$ m, $\rho = 1730$ kg/m³, with an internal friction angle of $\phi = 28^\circ$ and a bed friction angle of $\delta = 26^\circ$. The chute used in their experiments consisted of an inclined section at an angle of 60° with the shutter placed 1.448 m from the start of the curved transition zone (which had a radius of 0.246 m), followed by a 1.7-m runout zone. This allowed our simulation to be tested in isolation of the rolling resistance system described in the DEM formulation and for a much different chute geometry.

Figure 5 provides a comparison between the simulated slide dimensions and the data points recorded for the corresponding experiment in Fig. 22 of Hutter et al. (1995). The position distribution diagram highlights regions of greater thickness with increasing darkness in the vertical direction, not only allowing the slide front, peak, and tail positions to be determined, but also providing context on how steep the slide is throughout its length. While the initial condition could not be modelled exactly, a clear overall match can be seen between the predictions of the slide front, peak, and tail.

One of the main differences noted between the experiment of Hutter et al. (1995) and our simulation is the behaviour of the wedge immediately after shutter release. Figure 9 in Hutter et al. (1995) suggests that the wedge had cleared the shutter and entered a typical undisturbed slide profile by approximately $t = 0.15$ s from release. However, in the simulation, the wedge front took slightly longer to reach this standard profile, despite having fully detached from the shutter at this point. The shutter acceleration was calibrated such that

the shutter position matches between simulation and experiment at this point, implying that this effect must be related to the simulated particle dynamics. However, this difference had little effect on the bulk slide dynamics after the initial condition was resolved; the main difference being the time it took for the slide to fully run out, which could easily be adjusted by a constant to provide a better timing fit. Overall, the match seen in Fig. 5 is very good and better than that of the continuum model used in Hutter et al. (1995), or of the match between experiment 87 of Hutter et al. (1995) and the DEM simulations of Banton et al. (2009). In combination with the determination of suitable μ_r , η_r , and e values in the previous section, the simulation is validated and ready for comparison to the main chute experiments carried out using the new laboratory setup.

Results

The following section contains key data of the main scale series based on the new laboratory setup. Two different initial conditions were evaluated, with different slide surface angles θ_w and corresponding initial slide geometries (Table 1). These conditions were selected so that slides of different thicknesses and runout times could be compared to evaluate the DEM code. Data is shown for both the medium ($\lambda = 2$) and small ($\lambda = 4$) experimental scales. The simulation data shown is at the medium scale due to minimal differences found in comparison to other scales. The porosity of the initial laboratory release wedges was compared to the numerical simulation, with bulk values of $n = 0.38$ – 0.4 across both scales and initial conditions. This was significantly higher than the overall packing density measured in the final deposits, which showed values of $n = 0.48$ – 0.5 . In comparison, initial wedges in the numerical simulation displayed $n = 0.42$ – 0.44 , while simulated deposits showed values of $n = 0.5$ – 0.52 . No direct evidence of scale effects was seen in the calculated porosity or volume of the laboratory deposits.

Figure 6 provides a direct comparison between the experimental and simulated surface velocity (u_s) profiles for both conditions, with the experimental results being ensemble averaged for between 3 and 5 tests in each condition. It can be seen that the overall agreement is satisfactory for $\lambda = 2$; however, the simulation slightly overestimates u_s by up to 10% in some cases, with the slide front reaching each respective distance interval roughly 0.05–0.1 s before the experimental values. The simulated rate of velocity decrease (or deceleration) is roughly similar to the experimental rates seen, until the dispersive tail region is reached. Some differences between the simulation and experimental measurements are expected at the very front and in the dispersive tail, as these regions were observed to be those most affected by particle angularity and sphericity. Angular particles undergo more random collisions, resulting in the experimentally measured tails lasting for much longer with a very thin spread of particles that act independently with the ramp rather than as a granular slide. This can also be seen in a lesser extent at the slide front.

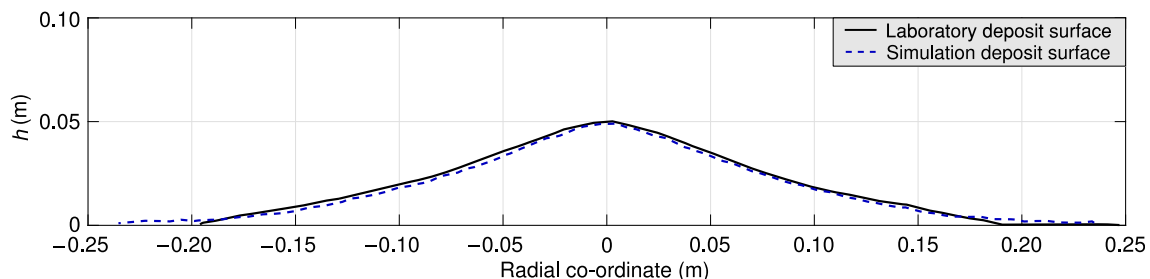


Fig. 3 Comparison of laboratory cylinder test deposit with simulation

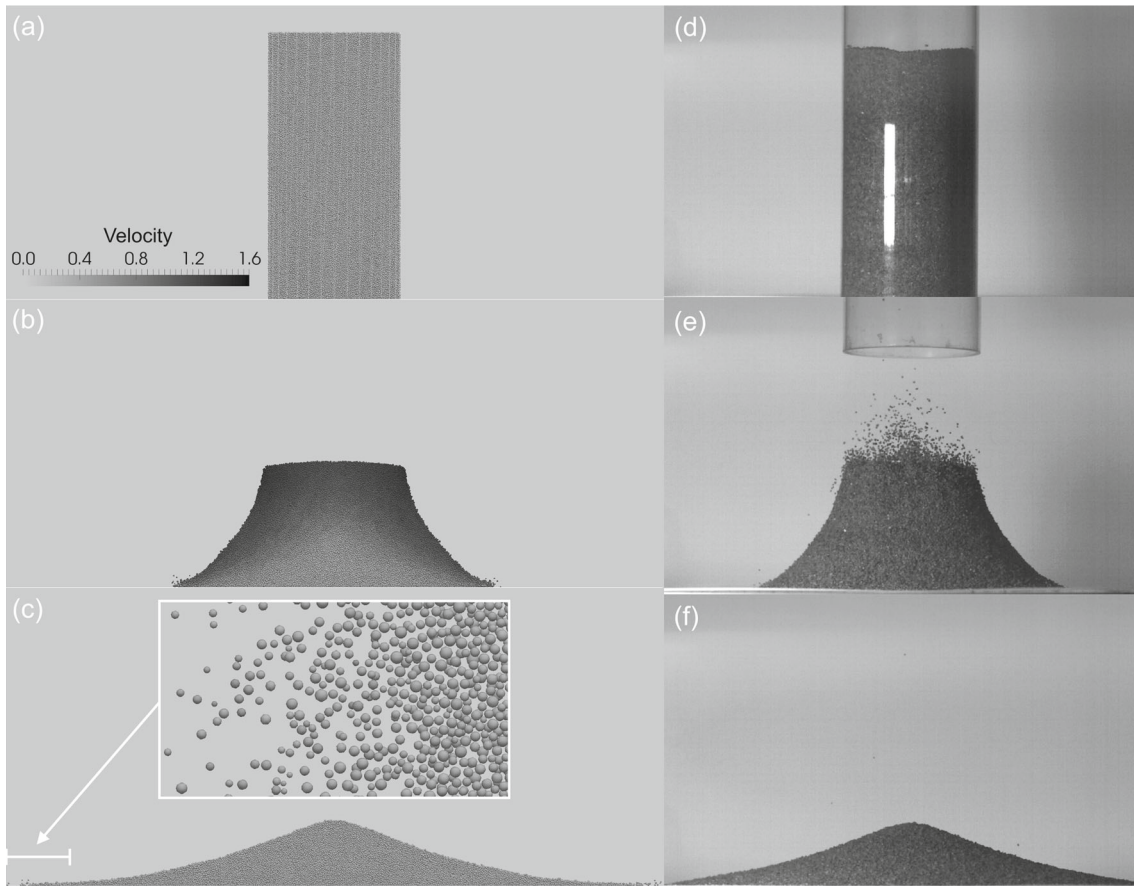


Fig. 4 Axisymmetric column collapse simulation at **a** $t = 0$ s, **b** $t = 0.283$ s, **c** $t = 0.552$ s (deposition complete) and **d–f** corresponding laboratory images. Subfigure in **c** indicates dilute boundary extent (radial coordinate < -0.2) in simulation

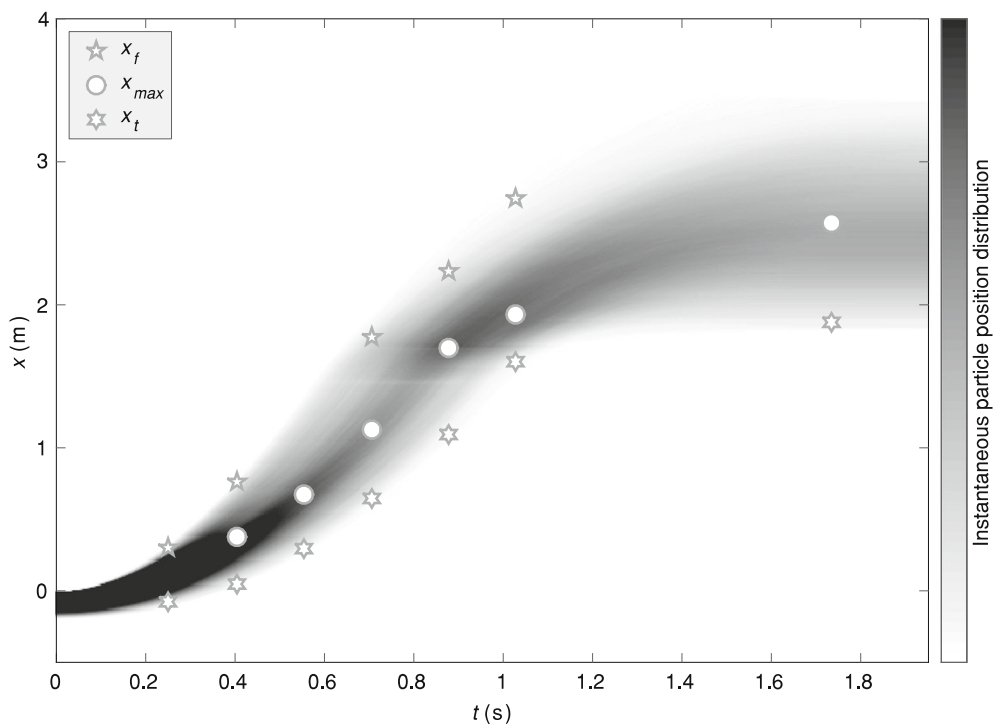


Fig. 5 Simulated (background) particle position distribution compared with x_f , x_{max} and x_t values from experiment 117 (symbols) of Hutter et al. (1995)

However, these shape effects do not appear to have as much influence on slide velocity for the main slide mass. Similar trends overall could be seen for both initial conditions, with the main differences being slightly increased surface flow velocities throughout the slide and slightly increased runout durations with greater θ_w .

The experimental data for $\lambda = 4$ shows some notable differences in Fig. 6; while the surface velocity seems to match the data quite well for $\lambda = 2$ at x_1 , a significant timing delay can still be seen. Meanwhile at x_2 , a clear decrease in surface velocity and corresponding increase in runout time through the measurement point can be seen. This indicates that scale effects present in the granular slide may be manifesting as the slide runs out and increases in velocity (and thus Re) and dust generation (an indirect consequence of the increased Ca), being negligible shortly after release but slowly becoming more and more dominant as the flow progresses. Furthermore, the surface velocity decrease is much sharper and occurs later in the slide for $\lambda = 4$ at both measurement points. These differences are consistent for both initial conditions and occur well before the front of the slide impacts with the transition curve. This maybe caused by the tail dispersion behaving differently at different scales; for $\lambda = 4$, the tail was seen to be more discrete, dissipating over less time relative to the tail at $\lambda = 2$. This is consistent with less turbulence being present at the smaller scale to stir up random motion in the tail, following expectations from calculated grain Reynolds numbers. As there is no large decrease in u_s measured at x_1 shortly after this contact time, this implies that this velocity decrease is not caused by a shock propagating up the ramp from the base level.

The thickness of the granular slide was also compared at x_1 and x_2 . Figure 7 shows a match of general patterns and values between the simulation and experimental data at $\lambda = 2$ for $\theta_w = 0^\circ$, with the thickness being overpredicted by up to 50% and the duration of runout being overestimated by 30% through x_1 and 40% through x_2 . This indicates that the simulated slide has a flatter flow surface that does not accumulate at the sides like in the experiments, or that the simulation did not accurately capture the change in flow thickness as the slide descends down the chute.

As Fig. 7 represents the flow thickness at a point over time, it is expected that the area underneath the simulated, faster flow does not match that of the measured, slower flow. The increased duration of runout through intervals is the main difference, with a well matching build-up to the peak interval thickness at a well matching initial time, but a much slower drop-off than in the experiments. This matches up with the behaviour seen in the validation in Fig. 4, as well as trends in the PIV velocity profiles (Fig. 6), which indicate the simulation overestimates flow velocities. In contrast, the experimental data at $\lambda = 4$ shows a decrease in overall slide thickness, particularly at the x_2 position. This is in addition to the delay in time of slide arrival at the measurement points as described previously. Again, this makes sense considering the lower grain Reynolds numbers of particles in the smaller scale experiments, where less turbulence is present to project particles further from the main slide mass, resulting in a more homogenous slide with a reduced overall thickness. The fluctuating component of the slide thickness was also increased in the experiments compared to the simulation, to a similar degree for both scales. While this can be partially attributed to angular particles forming a less continuous top layer of the slide, this could also be evidence of turbulence suspending this layer at both experimental scales.

Figure 8 compares the final deposits from laboratory experiments for two of the initial conditions (with repetitions displayed individually) to their respective simulations. Some notable differences between the simulated and experimental deposits can be seen. At $\lambda = 2$, the laboratory and simulated deposits show good agreement for lower values of θ_w in both overall shape and position of key parameters such as the slide peak, tail, and front. The simulation predicted a slide tail closer to the transition curve for higher values of θ_w , with the peak also being located closer to the slide tail. The deposit shows more agreement with the simulation closer to the sidewalls, with the laboratory tails varying significantly more across the channel width compared to the simulated counterparts. This indicates that sidewall friction effects were more prevalent in the experiments despite suitable friction angles being implemented and validated in the

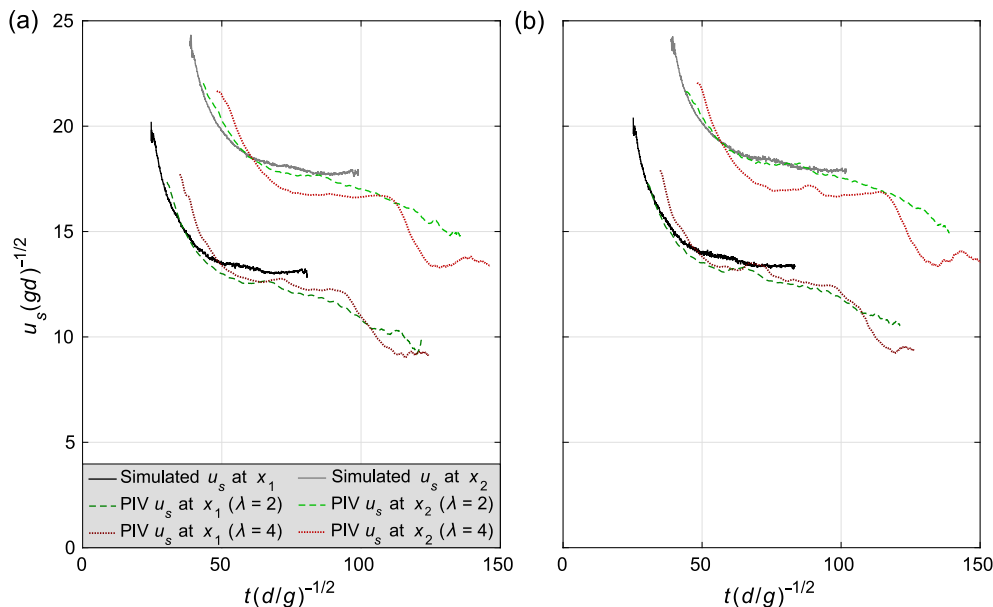


Fig. 6 Comparison of simulated and ensemble averaged experimental surface velocity profiles at release wedge surface angle **a** $\theta_w = 0^\circ$ and **b** $\theta_w = 7.5^\circ$

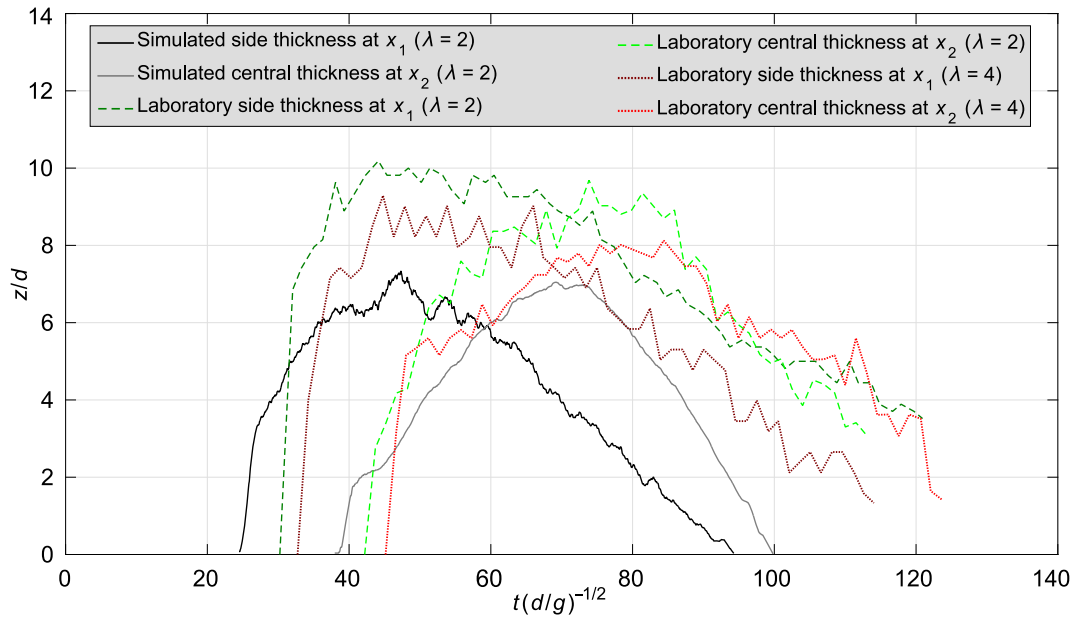


Fig. 7 Comparison of simulated and ensemble averaged experimental slide thickness at $x_1, y = -w/2$ and $x_2, y = 0$

simulation beforehand. This makes physical sense as the free surface of the slide is mixed by turbulence more than the sidewall flow surface in the experiments, resulting in a higher difference between the two surfaces than seen in the simulation. The laboratory data at $\lambda = 4$ shows significantly increased build-up in the transition curve region, resulting in a much higher slide peak, a less distant slide front, and an overall difference in deposit shape in comparison to the simulations. The large differences between the laboratory deposits at $\lambda = 2$ and $\lambda = 4$ may directly be attributed to scale effects.

Figure 9 compares the simulated front and tail positions and curvature to the experimental measurements, indicating that the simulation overpredicts the lateral spread and shallowness of the deposit front. This correlates with the data seen in the cylinder collapse validation in Fig. 3, showing that despite the tuneable parameters of the DEM being optimal for matching the bulk slide motion, free particles that disconnect from the bulk slide mass still have a tendency to roll further than expected. This may also be explained by the angularity of real particles preventing the top layer of the slide from flowing over the more settled base layer as effectively towards the end of the deposition phase, resulting in a

taller, shorter deposit mass. As this phenomenon was diminished in Fig. 3, it suggests that the geometry of the chute slide and the higher relative maximum particle velocities achieved in our configuration cause this spreading phenomenon to manifest more strongly than in the initial column collapse validation.

Table 2 shows measured values of Fr and Re for the conducted experiments. Some variation in measured Fr and Re can be seen for experiments at the same scale with different θ_w values. This information confirms that Re changes significantly with scale, showing that the dilute regions of the slide will be more turbulent for larger scales and thus subject to more randomness in particle contacts and overall behaviour. In contrast, the Froude number stays reasonably constant as expected in a Froude model. The scale effects seen may therefore be attributed mainly to differences in Re .

A DEM Froude scale series was conducted with the chute setup to evaluate the capacity of the simulation to capture scale effects. The medium-scale laboratory test ($\lambda = 2$) was used as a baseline, while a much larger simulation was ran at 10 times the scale ($\lambda = 0.2$). Further details are given in Tables 1 and 3. Figure 10 shows the evolution of the slide in the largest and smallest scales at four specific points in non-dimensionalised

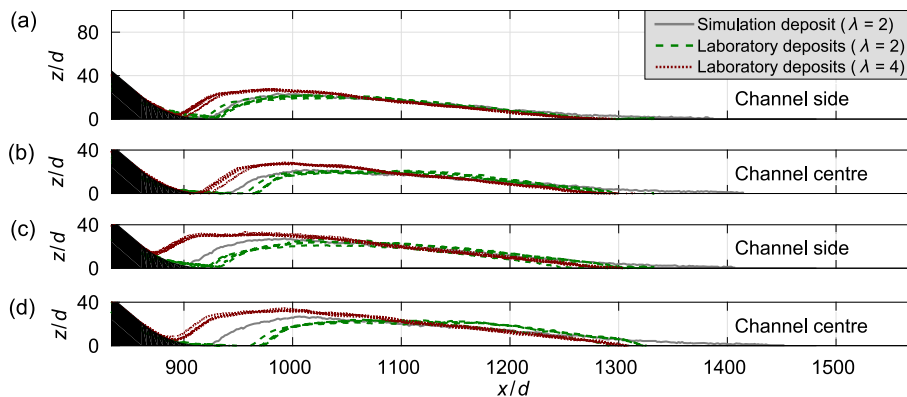


Fig. 8 Comparison of deposit surface profiles for a, b $\theta_w = 0^\circ$ and c, d $\theta_w = 7.5^\circ$

time ($t/\sqrt{d/g}$), with the initial slide tail and front positions marked as $x_{t,0}$ and $x_{f,0}$ respectively. The physical dimensions of the slide remain dimensionalised to clarify the presence of the two different scales. The overall behaviour of the slide remains very similar for both simulated scales at all important times in the slide's development, from soon after the slide initiation via the rotating shutter, during its pass over the transition curve, and to its final deposited state. No significant differences in flow velocity, thickness, or front and tail positions were discovered that could not be attributed to the random noise of particle collisions. Other secondary indicators of the slide behaviour, such as the curvature of the slide front and tail, as well as the extent and density of the dilute regime that detaches from the deposit front, also match between the two simulated scales. While this indicates that the simulations have been scaled effectively, it also indicates that the simulation fundamentally does not capture the scale effects seen in the experimental results even under more extreme scaling conditions than in the laboratory. This indicates that scale effects are indeed related to grain Reynolds number effects which are not considered in our DEM formulation, but are present in the laboratory experiments. Another potential explanation is increased dust generation and particle fracture with slide scale, which is addressed in more detail in the Discussion.

Discussion

Clear differences in slide behaviour showing the presence of scale effects can be seen in all of the experimental measurements at $\lambda = 4$ compared to both the simulation and experimental measurements at $\lambda = 2$. This may be caused by Re scale effects that may be present in the smaller experiments, which would imply that laboratory experiments at $\lambda = 1$ will continue this trend with increased slide velocities and runout distances. Low grain Reynolds numbers indicate viscous (i.e. velocity dependent) interaction between individual grains and the air, where large grain Reynolds numbers indicate turbulent form drag (which is velocity-squared dependent) between the particles and air (Jackson et al. 2013; Turnbull and McElwaine 2008; Turnbull et al. 2015). The type of drag has implications on other mechanisms within the flow such as fluidisation (which in turn can affect the basal friction on the slide) and internal energy dissipation (due to changes in porosity and collision networks). As Re decreases with λ , this implies that the reduction in turbulence surrounding the slide may be responsible for the decreased slide velocities and runout distances seen.

Another notable factor observed in the laboratory experiments was variance in dust generation and particle fracture, which is a model effect that is potentially caused by scale effects. Larger slides travel at higher speeds and with greater loads, meaning that the strength of individual particles at withstanding their specific loading conditions may become more important. While no evidence of dust generation was seen at $\lambda = 4$, there was some minor dust generation and particle breakage at $\lambda = 2$, particularly near the transition curve, where the intergranular stresses are at their highest. The volume of dust was very minor, in the order of 0.001–0.01% of the total slide mass, but it cannot be discounted entirely as a source of increasing flow velocity with scale. This may be linked to the Cauchy number, which also increases non-linearly with Froude scaling due to the constant E across all laboratory scales. Thus, it makes physical sense that particle breakage only starts to manifest in larger experiments when the particle compressibility and strength becomes more relevant, and extreme stress concentrations become more common. Particle abrasion and fracture could subtly alter the particle size distribution throughout the slide in different locations, or form fine dust that changes the macro-frictional properties of the material such as ϕ . This particle fracture may additionally help to mobilise the slide by reducing the mean energy dissipation of the slide, especially in the transition curve region.

No evidence of scale effects was seen in the calculated volume and porosity of the laboratory slide deposits, despite significant changes being seen in the measured front, peak, and tail positions and the overall shape of the deposits. However, the numerical simulations showed evidence of local porosity differing from those of the bulk mass. The variation of local porosity at key zones such as the transition curve and the deposit tail indicates a variation of stresses at different parts of the slide; these may be subject to scale effects in the laboratory experiments due to fluidisation effects not seen in our simulation. This supports the hypothesis of differences in local stress potentially being influenced by non-Reynolds-dependent scale effects seen in Iverson (2015). In particular, processes that affect the ratio $\sigma/\rho_s g h$ with the stress σ and slide density ρ_s (such as local dilation/contraction and shifting between collision- and contact-dominated behaviour) are still poorly understood, potentially causing scale effects that may be independent of Re.

Increased relative stress acting on the slide rear would justify the increase in rear runout distance seen in the larger experiments conducted,

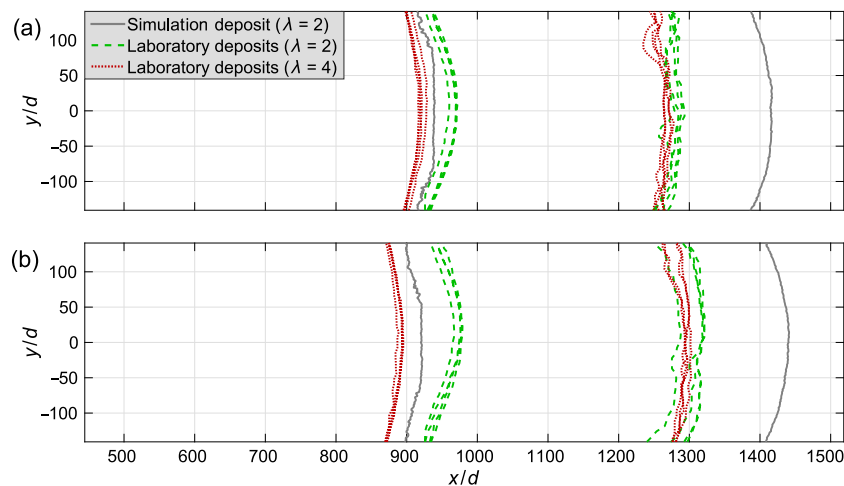


Fig. 9 Comparison of deposit front and tail positions for **a** $\theta_w = 0^\circ$ and **b** $\theta_w = 7.5^\circ$

and the smaller increase in front runout distance may be justified by these distant particles being less affected by this additional rear pressure as they are deposited. The simulation also showed an overall increase in initial slide porosity; this makes physical sense as the particles used in the laboratory had more angular shapes that could interlock more closely together. Notably, this difference seemed to mostly dissipate when comparing the final slide deposits, perhaps due to the overall reduced thickness of the deposit and the mixing and segregation process re-arranging particles into less tightly packed conditions throughout the slide.

Figure 9 shows that the simulated front distance exceeds the laboratory measurements at $\lambda = 2$ and 4 despite the angle of repose and rolling resistance being the same as those used in the column collapse, where a close match was observed. This indicates that there is a particular difference in the physics of the chute affecting the suitability of the particle shape modelling approach, such as the shock induced by the curved geometry, switching the flow from a Bagnold-like state into a more pronounced shear flow as the slide surface flows over a quasi-static core. The interlocking of angular particles may be responsible for this difference in behaviour, resulting in a more clustered and realistic chute deposit. It may be possible that this rolling resistance approach is more suitable for slower particles and more confined slide geometries than for faster, shallower slides, where the particle contact eccentricity is more likely to vary due to both the increased particle velocities and increased time to run out. On the other hand, it is also known that the rolling resistance coefficient depends on the particle loading (Ai et al. 2011), which is clearly smaller in the column collapse than in the chute simulations.

Overall, there was little evidence of scale effects seen in the numerical simulations, as seen in Fig. 10. This highlights the importance of combining this numerical approach with experiments, to see whether scale effects can be produced in experimental scale series and how these may not be captured numerically. Another possible explanation for the lack of observing scale effects is that many slide characteristics may become Re invariant in the turbulent regime, as similarly observed in fluid flows (Heller 2017). The invariance would imply that no Re scale effects are involved; given that the majority of scale effects are expected to occur due to changes in Re, this would justify the minor differences seen in Fig. 10. Self-similarity (Andreotti et al. 2013; Barenblatt 1996; Heller 2017) is another common concept which could explain scale invariance and therefore insignificant scale effects. However, whether these concepts also apply to the granular slides analysed herein and at which Re remains open for future research.

Conclusions

A laboratory-numerical approach has been applied and tested for capturing scale effects in granular slides in a chute configuration at a variety of different scales. Laboratory experiments with Froude similarity were completed for different slide geometries and scales, with key parameters such as the slide velocity, thickness, and runout time being recorded. Discrete element method (DEM) using LIGGGHTS code has been validated and calibrated through both an axisymmetric column collapse and a comparison to an experiment from Hutter et al. (1995) using spherical particles, before being used to model our main tests. This model used a rolling resistance method of applying counter-active torque to spherical particles to accurately and cheaply simulate the effects of particle shape on bulk slide dynamics, with this model proving successful in the column collapse test in particular.

Overall, clear scale effects can be seen in the experimental results, both in the slide's behaviour as it develops and in its final deposit patterns. These scale effects can mainly be attributed to differences in the Reynolds number (Re) between experiments of different scales. Particle image velocity (PIV) measurements indicate that this divergence in behaviour may start midway through the slide event, with the small scale slide ($\lambda = 4$) velocity increasing less quickly than that of the medium-scale slide ($\lambda = 2$) towards the bottom of the ramp. Increased runout distance and decreased build-up in the ramp's transition curve can also be seen at the larger of the two scales. While the numerical model captures the properties of the slide well at $\lambda = 2$, it fails to replicate these scale effects when looking at a much larger granular slide of $\lambda = 0.2$. This may be due to the μ_r rolling resistance model used to simulate particle roughness not capturing important grain-scale details that affect the macroscopic flow. Similarly, this may be due to Reynolds-dependent phenomena such as turbulent particle mixing being present in the experiments but not in the simulation. Dust generation and particle fracture mechanisms are also not incorporated, ignoring a potential source of scale effects related to the Cauchy number (Ca). Alternatively, there may be inherent differences caused in the DEM engine, such as the use of a spring-dashpot contact model, that may prevent important processes from being captured. These factors all reinforce the importance of using laboratory experiments to capture scale effects.

Further laboratory experiments will be conducted with a scale factor of $\lambda = 1$ to further evaluate the influence of scale effects in real granular slides and to identify whether the numerical simulation is accurately modelling these scale effects. Smaller simulations will also be run up to $\lambda = 20$ to verify that the scaling issue is

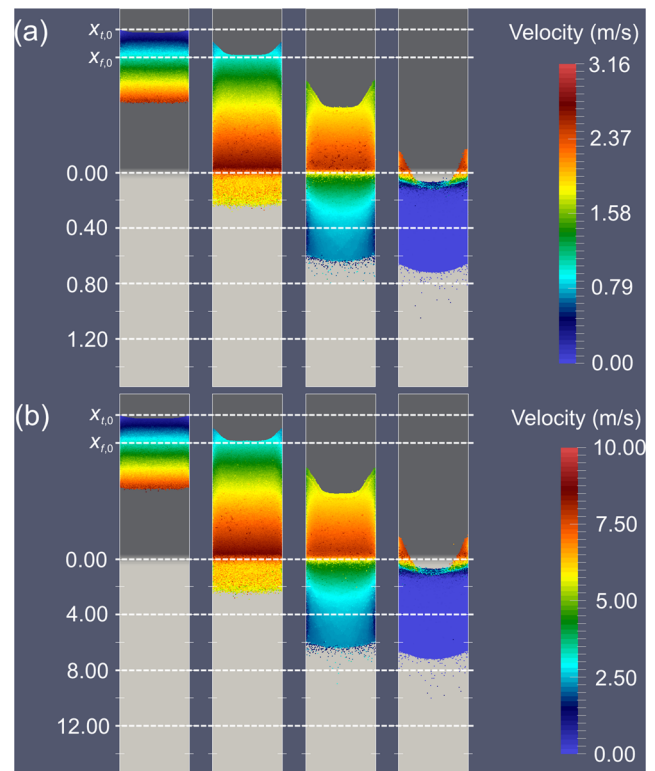


Fig. 10 Simulated scale series indicating slide positions and velocities at a $\lambda = 2$ and **b** $\lambda = 0.2$. Images taken from left to right at $t/\sqrt{d/g} = 28.6, 57.2, 85.8,$ and 114.4 respectively for both scales

present in both scaling directions. The effects of air flow on granular slide numerical modelling and scaling may also be evaluated, by coupling the LIGGGHTS code with a computational fluid dynamics (CFD) code (Shan and Zhao 2014).

Acknowledgements

The authors would like to thank Mr. Steven Gange and Mr. Balbir Loyla for their assistance and expertise in preparing the experimental setup, as well as Dr. Nikolaos Kokkas for providing advice on photogrammetry techniques. Prof. Stuart Marsh is acknowledged for providing advice throughout this study and providing access to the AgiSoft photogrammetry software. The simulations were conducted on the HPC cluster Minerva. This work was supported by the Engineering and Physical Sciences Research Council [grant number EP/M506588/1] (EPSRC).

Nomenclature a , acceleration vector; Ca , Cauchy number; Ca_b , initial Cauchy number; d , mean grain diameter; e , coefficient of restitution; E , particle Young's modulus; Eu , Euler number; f , data capture frequency; F_b , body force vector; F_n , normal force vector; F_t , tangential force vector; Fr , Froude number; Fr_b , initial Froude number; g , gravitational acceleration; h , slide thickness; h_{max} , maximum slide thickness along center line; H_c , height of slide mass centroid above runout area; $H_{s,0}$, initial slide thickness at shutter position; I , moment of inertia; k_n , normal spring coefficient; k_t , tangential spring coefficient; L_r , length of inclined ramp section; $L_{s,0}$, initial slide length; L_{sh} , distance of axis of rotation from ramp surface; m , particle mass; M , slide mass; n , porosity; n_p , number of particles in simulation; r_c , particle radius contact vector; R , radius of ramp transition; R_p , effective rolling radius of particle contact; Re , grain Reynolds number; Re_b , initial grain Reynolds number; t , time; $t_{c,0}$, time of particle contact; t_s , simulation time step; T_r , slide runout completion time; $T_{r,real}$, real time for simulated slide runout; T_s , settlement time; $T_{s,real}$, real time for simulated settlement; T_r , rolling resistance torque; T_r^k , mechanical spring rolling resistance torque; T_r^d , viscous damping rolling resistance torque; $T_{r,max}$, maximum rolling resistance torque; u , slide velocity; u_b , initial characteristic slide velocity; u_s , rampwise slide surface velocity; $u_{x,0}$, rampwise component of slide velocity; v_s , shutter-tip velocity; V , slide volume; w , channel width; x , rampwise position coordinate along channel length; x_f , rampwise position of slide front; $x_{f,0}$, initial rampwise position of slide front; x_{max} , rampwise position of slide peak; x_b , rampwise position of slide tail; $x_{t,0}$, initial rampwise position of slide tail; x_1 , first measurement position along channel length; x_2 , second measurement position along channel length; y , rampwise position coordinate across channel length; z , rampwise position coordinate above channel surface; δ , bed friction angle; δ_m , particle overlap distance; η , rolling viscous damping ratio; Δu_n , relative normal velocity at contact point; Δu_t , relative tangential velocity at contact point; γ_n , normal damping coefficient; γ_t , tangential damping coefficient; λ , scale factor; μ , friction coefficient; μ_r , coefficient of rolling resistance; ν , kinematic viscosity; ω , particle rotational velocity vector; ω_s , shutter angular acceleration; ϕ , internal friction angle; ρ , grain density; ρ_s , slide density; σ , stress; θ_b , angle between laser and ramp surface; θ_R , ramp angle; θ_{w3} , release wedge surface angle

Open Access This article is distributed under the terms of the Creative Commons Attribution 4.0 International License (<http://creativecommons.org/licenses/by/4.0/>), which permits unrestricted use, distribution, and reproduction in any medium, provided you give appropriate credit to the original author(s) and the

source, provide a link to the Creative Commons license, and indicate if changes were made.

References

- AgiSoft-LLC (2016) Agisoft Photoscan Professional (Version 1.2.6). Retrieved from <http://www.agisoft.com/downloads/installer/>. Accessed 13 June 2017
- Ai J, Chen J-F, Rotter JM, Ooi JY (2011) Assessment of rolling resistance models in discrete element simulations. *Powder Technol* 206(3):269–282
- Andreotti B, Forterre Y, Pouliquen O (2013) *Granular media: between liquid and solid*. Cambridge University Press, New York
- Aradian A, Raphaël E, de Gennes P-G (2002) Surface flows of granular materials: a short introduction to some recent models. *C R Phys* 3:187–196
- Armanini A (2013) Granular flows driven by gravity. *J Hydraul Res* 51(2):111–120
- Bagnold RA (1954) Experiments on a gravity-free dispersion of large solid spheres in a Newtonian fluid under shear. *Proc R Soc A* 225(1160):49–63
- Banton J, Villard P, Jongmans D, Scavia C (2009) Two-dimensional discrete element models of debris avalanches: parameterization and the reproducibility of experimental results. *J Geophys Res* 114(F04013):1–15
- Barenblatt GI (1996) *Scaling, self-similarity, and intermediate asymptotics*. Cambridge University Press, Cambridge
- Börszönyi T, Ecke RE, McElwaine JN (2009) Patterns in flowing sand: understanding the physics of granular flow. *Phys Rev Lett* 103(178302):1–4
- Bryant SK, Take WA, Bowman ET (2014) Observations of grain-scale interactions and simulation of dry granular flows in a large-scale flume. *Can Geotech J* 52(5):638–655
- Bui HH, Fukagawa R, Sako K, Ohno S (2008) Lagrangian meshfree particles method (SPH) for large deformation and failure flows of geomaterial using elastic-plastic soil constitutive model. *Int J Numer Anal Methods Geomech* 32(12):1537–1570
- Campbell CS (2011) Elastic granular flows of ellipsoidal particles. *Phys Fluids* 23:013306
- Chang DS, Zhang LM, Xu Y, Huang R (2011) Field testing of erodibility of two landslide dams triggered by the 12 May Wenchuan earthquake. *Landslides* 8(3):321–332
- Choi CE, Ng CWW, Au-Yeung SCH, Goodwin GR (2015) Froude characteristics of both dense granular and water flows in Froude modelling. *Landslides* 12(6):1197–1205
- Cleary PW, Frank M (2006) Three-dimensional discrete element simulations of axisymmetric collapses of granular columns. Technical Report 44710, Technische Universität Kaiserslautern
- Collins GS, Melosh HJ (2003) Acoustic fluidization and the extraordinary mobility of sturzstroms. *J Geophys Res* 108(B10). <https://doi.org/10.1029/2003JB002465>
- Cundall PA, Strack ODL (1979) A discrete numerical model for granular assemblies. *Geotechnique* 29(1):47–65
- Dalziel SB (2009) Digiflow user guide, Dalziel research partners. Retrieved from <http://www.dalzielresearch.com/digiflow/digiflow.htm/>. Accessed 27 June 2017
- Davies TR, McSaveney MJ, Hodgson KA (1999) A fragmentation-spreading model for long-runout rock avalanches. *Can Geotech J* 36(6):1096–1110
- Eckart W, Gray JMNT, Hutter K (2003) *Particle image velocimetry (PIV) for granular avalanches on inclined planes*. Springer-Verlag, Berlin
- Erismann TH (1986) Flowing, rolling, bouncing, sliding: synopsis of basic mechanisms. *Acta Mech* 64(1):101–110
- Glimsdal S, L'Heureux JS, Harbitz CB, Løvholt F (2016) The 29th January 2014 submarine landslide at Statland, Norway—landslide dynamics, tsunami generation, and run-up. *Landslides* 13(6):1435–1444
- Gray JMNT, Edwards AN (2014) A depth-averaged $\mu(I)$ -rheology for shallow granular free-surface flows. *J Fluid Mech* 755:503–534
- Grima A, Wypych PW (2011) Development and validation of calibration methods for discrete element modelling. *Granul Matter* 13:127–132
- Haque U, Blum P, da Silva PF, Andersen P, Pilz J, Chalov SR et al (2016) Fatal landslides in Europe. *Landslides* 13(6):1545–1554
- Heller V (2011) Scale effects in physical hydraulic engineering models. *J Hydraul Res* 49(3):293–306
- Heller V (2017) Self-similarity and Reynolds number invariance in Froude modelling. *J Hydraul Res* 55(3):293–309
- Heller V, Hager WH, Minor H-E (2008) Scale effects in subaerial landslide generated impulse waves. *Exp Fluids* 44(5):691–703
- Hertz H (1882) Über die Berührung fester elastischer Körper (on the contact of elastic solids). *J Reine Angewandte Math* 94:156–171, (English translation in *Miscellaneous Papers by Hertz, H. (ed.) Jones and Schott, London, Macmillan, 1896*)
- Houlsby GT (2009) Potential particles: a method for modelling non-circular particles in DEM. *Comput Geotech* 36:953–959

- Hutter K, Koch T, Plüss C, Savage SB (1995) The dynamics of avalanches of granular materials from initiation to runout. Part II. Experiments. *Acta Mech* 109(1–4):127–165
- Iverson RM (2015) Scaling and design of landslide and debris-flow experiments. *J Geophys Res* 244:9–20
- Iverson RM, Logan M, LaHusen RG, Berti M (2010) The perfect debris flow? Aggregated results from 28 large-scale experiments. *J Geophys Res* 115(F03005):1–29
- Jackson AJ, Turnbull B, Munro R (2013) Scaling for lobe and cleft patterns in particle-laden gravity currents. *Nonlinear Process Geophys* 20:121–130
- Johnson BC, Campbell CS, Melosh HJ (2016) The reduction of friction in long runout landslides as an emergent phenomenon. *J Geophys Res Earth Surf* 121(5):1–8
- Juanico DE, Longjas A, Batac R, Monterola C (2008) Avalanche statistics of driven granular slides in a miniature mound. *Geophys Res Lett* 35(L19403):1–4
- Kloss C, Goniya C, Hager A, Amberger S, Pirker S (2012) Models, algorithms and validation for open-source DEM and CFD-DEM. *Prog Comput Fluid Dyn* 12(2/3):140–152
- Kruggel-Emden H, Rickett S, Wirtz S, Scherer V (2008) A study on the validity of the multi-sphere discrete element method. *Powder Technol* 188:153–165
- Lajeunesse E, Mangeney-Castelnau A, Vilotte JP (2004) Spreading of a granular mass on a horizontal plane. *Phys Fluids* 16(7):2371–2381
- Latham J-P, Munjiza A (2004) The modelling of particle systems with real shapes. *Phil Trans R Soc A* 362(1822):1953–1972
- LIGGGHTS (2016) Gran model hertz model. DCS Computing GmbH, JKU Linz and Sandia Corporation. Retrieved from https://www.cfdem.com/media/DEM/docu/gran_model_hertz.html. Accessed 26 June 2017
- Liu L (2003) Simulation of microstructural evolution during isostatic compaction of monosized spheres. *J Phys D* 36:1881–1889
- Liu W, He S, Li X, Xu Q (2016) Two-dimensional landslide dynamic simulation based on a velocity-weakening friction law. *Landslides* 13(5):957–965
- Llano-Serna MA, Farias MM, Pedroso DM (2016) An assessment of the material point method for modelling large scale run-out processes in landslides. *Landslides* 13(5):1057–1066
- Loth E (2008) Drag of non-spherical solid particles of regular and irregular shape. *Powder Technol* 182(3):342–353
- Lube G, Huppert HE, Sparks RSJ, Hallworth MA (2004) Axisymmetric collapses of granular columns. *J Fluid Mech* 508:175–199
- Lucas A, Mangeney A, Ampuero JP (2014) Frictional velocity-weakening in landslides on Earth and on other planetary bodies. *Nat Commun* 5(3417)
- Markauskas D, Kačianauskas R (2011) Investigation of rice grain flow by multi-sphere particle model with rolling resistance. *Granul Matter* 13(2):143–148
- Matsushima T, Saomoto H (1978) Discrete element modeling for irregularly shaped sand grains. In: Proc. NUMGE2002: numerical methods in geotechnical engineering, pp 239–246
- McElwaine JN, Nishimura K (2001) Ping-pong ball avalanche experiments. Blackwell Publishing Ltd, Oxford
- MiDi GDR (2004) On dense granular flows. *Eur Phys J E* 14(4):341–365
- Mirghasemi AA, Rothenburg L, Matyas EL (1997) Numerical simulations of assemblies of two-dimensional polygon-shaped particles and effects of confining pressure on shear strength. *Soils Found* 37(3):43–52
- Mollanouri Shamsi MM, Mirghasemi AA (2012) Numerical simulation of 3d semi-real-shaped granular particle assembly. *Powder Technol* 221:431–446
- Montrasio L, Schiliro L, Terrone A (2016) Physical and numerical modelling of shallow landslides. *Landslides* 13(5):873–883
- Nguyen CT, Bui HH, Nguyen GD, Fukugawa R (2017) A new SPH-based approach to simulation of granular flows using viscous damping and stress regularisation. *Landslides* 14(1):69–81
- Oudafel H (1998) Numerical simulation of granular assemblies with three-dimensional ellipsoid-shaped particles. PhD thesis, Department of Civil Engineering, Waterloo University, Ontario
- Parez S, Aharonov E (2015) Long runout landslides: a solution from granular mechanics. *Front Phys* 3(80):1–10
- Pouliquen O, Forterre Y (2009) A non-local rheology for dense granular flows. *Phil Trans R Soc A* 367(1909):5091–5107
- Pudasaini SP, Hutter K (2010) *Avalanche dynamics: dynamics of rapid flows of dense granular avalanches*. Springer-Verlag, Berlin
- Reddy KA, Kumaran V (2010) Dense granular flow down an inclined plane: a comparison between the hard particle model and soft particle simulations. *Phys Fluids* 22(113302):1–24
- Saingier G, Deboeuf S, Lagrée P-Y (2016) On the front shape of an inertial granular flow down a rough incline. *Phys Fluids* 28(053302). <https://doi.org/10.1063/1.4948401>
- Savage SB, Hutter K (1989) The motion of a finite mass of granular material down a rough incline. *J Fluid Mech* 199:177–215
- Shan T, Zhao J (2014) A coupled CFD-DEM analysis of granular flow impacting on a water reservoir. *Acta Mech* 225(8):2449–2470
- Silbert LE, Grest GS, Plimpton SJ, Levine D (2002) Boundary effects and self-organization in dense granular flows. *Phys Fluids* 14:2637–2645
- Sukumaran B, Ashmawy AK (2001) Quantitative characterisation of the geometry of discrete particles. *Geotechnique* 51:1–9
- Thielicke W, Stamhuis EJ (2014) PIVlab: towards user-friendly, affordable and accurate digital particle image velocimetry in MATLAB. *J Open Res Softw* 2(1):1–10
- Thompson EL, Huppert HE (2007) Granular column collapses: further experimental results. *J Fluid Mech* 575:177–186
- Thornton C (2015) *Granular dynamics, contact mechanics and particle system simulations*. Springer International Publishing, Switzerland
- Turnbull B (2011) Scaling laws for melting ice avalanches. *Phys Rev Lett* 107(258001):1–4
- Turnbull B, McElwaine JN (2008) Experiments on the non-Boussinesq flow of self-igniting suspension currents on a steep open slope. *J Geophys Res* 112(F000753)
- Turnbull B, Bowman ET, McElwaine JN (2015) Debris flows: experiments and modelling. *C R Phys* 16(1):86–96
- Verlet L (1967) Computer “experiments” on classical fluids. Part I. Thermodynamical properties of Lennard-Jones molecules. *Phys Rev* 159(1):98–103
- Wadell H (1932) Volume, shape, and roundness of rock particles. *J Geol* 40:443–451
- Walton O (1982) Discrete element analysis of granular materials. In: Proc. 4th International Conference of Numerical Methods in Geomechanics, Balkema, Rotterdam, pp 1799–1803
- Warnett JM, Denissenko P, Thomas PJ, Kiraci E, Williams MA (2014) Scalings of axisymmetric granular column collapse. *Granul Matter* 16:115–124
- Wensrich CM, Katterfeld A (2012) Rolling friction as a technique for modelling particle shape in DEM. *Powder Technol* 217:409–417
- Whitehead AN, Russell B (1912) *Principia Mathematica: Vol II*. University Press, Cambridge
- Więckowski Z, Youn S-K, Yeon J-H (1999) A particle-in-cell solution to the silo discharging problem. *Int J Numer Methods Eng* 45(9):1203–1225
- Wu CY, Cocks A (2006) Numerical and experimental investigations of the flow of powder into a confined space. *Mech Mater* 38(4):304–324
- Wu F, Fan Y, Liang L, Wang C (2016) Numerical simulation of dry granular flow impacting a rigid wall using the discrete element method. *PLoS One* 11(8):1–17
- Xu C, Xu X, Yao X, Dai F (2014) Three (nearly) complete inventories of landslides triggered by the May 12, 2008 Wenchuan Mw 7.9 earthquake of China and their spatial distribution statistical analysis. *Landslides* 11(3):441–461
- Yavari-Ramshe S, Ataie-Ashtiani B (2016) Numerical modelling of subaerial and submarine landslide-generated tsunami waves—recent advances and future challenges. *Landslides* 13(6):1325–1368
- Yu AB, An XZ, Zou RP, Yang RY, Kendall K (2006) Self-assembly of particles for densest packing by mechanical vibration. *Phys Rev Lett* 97(265501):1–8
- Zhang X, Vu-Quoc L (2000) Simulation of chute flow of soybeans using an improved tangential force–displacement model. *Mech Mater* 32:115–129
- Zhao T (2017) *Coupled DEM-CFD analyses of landslide-induced debris flows*. Springer Nature, Singapore
- Zheng J, Hryciw RD (2017) An image based clump library for DEM simulations. *Granul Matter* 14:229–234
- Zhu HP, Zhou ZY, Yang RY, Yu AB (2007) Discrete particle simulation of particulate systems: theoretical developments. *Chem Eng Sci* 62:3378–3396
- Zhu HP, Zhou ZY, Yang RY, Yu AB (2008) Discrete particle simulation of particulate systems: a review of major applications and findings. *Chem Eng Sci* 63:5728–5770

M. Kessler (✉) · V. Heller · B. Turnbull

University of Nottingham,
Nottinghamshire, Nottingham, UK
Email: matthew.kessler@nottingham.ac.uk

V. Heller

e-mail: valentin.heller@nottingham.ac.uk

B. Turnbull

e-mail: barbara.turnbull@nottingham.ac.uk